

ACCEPTED MANUSCRIPT

Electronic structures of vacancies in $\text{Co}_3\text{Sn}_2\text{S}_2$ To cite this article before publication: Yuxiang Gao *et al* 2021 *Chinese Phys. B* in press <https://doi.org/10.1088/1674-1056/abfa05>

Manuscript version: Accepted Manuscript

Accepted Manuscript is “the version of the article accepted for publication including all changes made as a result of the peer review process, and which may also include the addition to the article by IOP Publishing of a header, an article ID, a cover sheet and/or an ‘Accepted Manuscript’ watermark, but excluding any other editing, typesetting or other changes made by IOP Publishing and/or its licensors”

This Accepted Manuscript is © 2021 Chinese Physical Society and IOP Publishing Ltd.

During the embargo period (the 12 month period from the publication of the Version of Record of this article), the Accepted Manuscript is fully protected by copyright and cannot be reused or reposted elsewhere.

As the Version of Record of this article is going to be / has been published on a subscription basis, this Accepted Manuscript is available for reuse under a CC BY-NC-ND 3.0 licence after the 12 month embargo period.

After the embargo period, everyone is permitted to use copy and redistribute this article for non-commercial purposes only, provided that they adhere to all the terms of the licence <https://creativecommons.org/licenses/by-nc-nd/3.0>

Although reasonable endeavours have been taken to obtain all necessary permissions from third parties to include their copyrighted content within this article, their full citation and copyright line may not be present in this Accepted Manuscript version. Before using any content from this article, please refer to the Version of Record on IOPscience once published for full citation and copyright details, as permissions will likely be required. All third party content is fully copyright protected, unless specifically stated otherwise in the figure caption in the Version of Record.

View the [article online](#) for updates and enhancements.

Electronic structures of vacancies in $\text{Co}_3\text{Sn}_2\text{S}_2$ *

Yuxiang Gao(高于翔)¹, Xin Jin(金鑫)¹, Yixuan Gao(高艺璇)¹, Yu-Yang Zhang(张余洋)^{1,2,†}, and Shixuan Du(杜世萱)^{1,2,3,4,‡}

¹ *Institute of Physics and University of Chinese Academy of Sciences, Chinese Academy of Sciences, Beijing 100190, PR China*

² *CAS Center for Excellence in Topological Quantum Computation, University of Chinese Academy of Sciences, Beijing 100190, PR China*

³ *Beijing National Center for Condensed Matter Physics, Beijing 100190, PR China*

⁴ *Songshan Lake Materials Laboratory, Dongguan, Guangdong 523808, PR China*

$\text{Co}_3\text{Sn}_2\text{S}_2$ has attracted a lot of attention for its multiple novel physical properties, including topological nontrivial surface states, anomalous Hall effect, and anomalous Nernst effect. Vacancies, which play important roles in functional materials, have attracted increasing research attention. In this paper, by using density functional theory calculations, we first obtain band structures and magnetic moments of $\text{Co}_3\text{Sn}_2\text{S}_2$ with exchange-correlation functionals at different levels. It is found that the generalized gradient approximation gives the positions of Weyl points consistent with experiments in bulk $\text{Co}_3\text{Sn}_2\text{S}_2$. We then investigate the electronic structures of defects on surfaces with S and Sn terminations which have been observed in experiments. The results show that the single sulfur vacancy on the S-terminated surface introduces localized bond states inside the bandgap near the Fermi level. For di- and tri-sulfur vacancies, the localized defect states hybridize with neighboring ones, forming bonding states as well as anti-bonding states. The Sn vacancy on the Sn-terminated surface also introduces localized bond states, which are merged with the valence bands. These results provide a reference for future experimental investigations of vacancies in $\text{Co}_3\text{Sn}_2\text{S}_2$.

Keywords: first-principle calculations, vacancies, localized bound states, orbital hybridization

PACS: 71.15.Mb Density-functional theory (condensed matter), 61.72.Jd Vacancies in crystals, 71.55.Ak Impurity and defect levels in semimetals, 71.70.-d Level

* Project supported by National Key R&D program of China (Nos. 2019YFA0308500 and 2018YFA0305800), National Natural Science Foundation of China (Nos. 51922011 and 61888102), Strategic Priority Research Program of the Chinese Academy of Sciences (Nos. XDB30000000 and XDB28000000), and the Fundamental Research Funds for the Central Universities.

† Corresponding author. E-mail: zhangyuyang@ucas.ac.cn ‡ Corresponding author. E-mail: sxdu@iphy.ac.cn

splitting in solids

1. Introduction

$\text{Co}_3\text{Sn}_2\text{S}_2$, a newly discovered Weyl semimetal, has received much attention in recent years^[1-7]. Different from other Weyl semimetals such as TaAs, TaP, NbAs, and NbP reported earlier^[8-10], $\text{Co}_3\text{Sn}_2\text{S}_2$ has intrinsic magnetism and thus breaks time-reversal symmetry^[11-14]. Fermi arcs and Weyl nodes in this material have been observed under an external magnetic field and finely tuned through the control of magnetization^[1, 15-19]. Moreover, because the position of Weyl nodes in $\text{Co}_3\text{Sn}_2\text{S}_2$ are close to the Fermi level, a large intrinsic anomalous Hall effect was predicted and experimentally observed^[20-25]. Besides, multiple novel physical properties were also observed, including anomalous Nernst effect^[26-28] and anisotropic negative magnetoresistance^[25].

Defects play key roles in a wide range of materials because they are inevitable in real materials and notably influence the physical properties of the hosts^[29-35]. The defects in GaN significantly affect its electrical and optical properties, seriously degrading the performance and reliability of devices^[32, 33]. While several types of defects were found to increase the catalytic performance for the hydrogen evolution reaction^[34, 35], carbon dioxide reduction reaction^[36], and photocatalytic reaction^[37]. Very recently, it is found that a substituted indium impurity in $\text{Co}_3\text{Sn}_2\text{S}_2$ introduces a striking localized bound state^[38]. Besides, single S vacancies in a S-terminated surface introduce spin-orbit polaron^[39]. Thus, a theoretical study of the electronic structures of various defects in $\text{Co}_3\text{Sn}_2\text{S}_2$ is necessary for future experimental investigations.

In this paper, using quantum mechanical calculations based on density functional theory (DFT), we calculate the band structures and magnetic properties of bulk $\text{Co}_3\text{Sn}_2\text{S}_2$ with several functionals at different levels. It is found that the positions of Weyl nodes and the magnetic moments given by generalized gradient approximation (GGA) implemented by Perdew-Burke-Ernzerhof (PBE) are consistent with the reported experimental results. While Heyd-Scuseria-Ernzerhof screened hybrid

functional (HSE06) highly overestimates the magnetic moments and a gap is found near the Fermi level, which is different from the semimetal nature of $\text{Co}_3\text{Sn}_2\text{S}_2$. We then exploit PBE functional to further investigate the electronic structures and formation energies of defects on S-terminated and Sn-terminated surfaces. We found that vacancies in the S-terminated surface have a significant influence on its band topology. A single sulfur vacancy (V_S) induces spin-polarized localized bond states in the gap near the Fermi level. When two or three S vacancies approached, they interact with each other. The localized states hybridize and form bonding states as well as anti-bonding states. For the Sn vacancy on the Sn-terminated surface, the defect levels are not found in the gap near the Fermi level but are merged with the valence bands. These results may help to understand this compound more comprehensively and would be beneficial for further investigations.

2. Methods

First-principle calculations based on density functional theory (DFT) were performed by using the Vienna Ab initio Simulation Package (VASP) [40, 41]. The projector augmented wave (PAW) [42] method was applied. Exchange-correlation functionals at different levels were used, including local density approximation (LDA), Perdew–Burke–Ernzerhof (PBE) [43], modified Becke-Johnson (mBJ) [44, 45], and Heyd-Scuseria-Ernzerhof screened hybrid functional (HSE06) [46]. A kinetic energy cutoff of 400 eV was used for bulk and pristine surfaces calculations. A kinetic energy cutoff of 270 eV was used for surfaces with defects.

A primitive cell of bulk $\text{Co}_3\text{Sn}_2\text{S}_2$ contains 3 Co atoms, 2 Sn atoms, and 2 S atoms in a rhombohedral crystal structure (R-3m). The slab models containing six Co-Sn layers and extra S, Sn, and Co_3 -Sn layers were used to simulate the S-terminated, Sn-terminated, and Co-terminated surfaces, respectively. Single vacancies were simulated in 4×4 supercells, while two or three vacancies were simulated in 5×5 supercells. For structural relaxations, the atoms between the middle two Co_3 -Sn layers

were constrained and other atoms were fully relaxed. The vacuum layers of the slab models were larger than 15 Å.

For bulk $\text{Co}_3\text{Sn}_2\text{S}_2$, the k-points sampling was $8 \times 8 \times 8$, generated by Monkhorst-Pack grids with the origin at the Γ -point^[47]. For pristine S-terminated, Sn-terminated, and Co-terminated surfaces of $\text{Co}_3\text{Sn}_2\text{S}_2$, the k-points sampling was $8 \times 8 \times 1$. For surfaces with vacancies, the k-points sampling was only the Γ -point. The structures were relaxed until the residual force on each atom was smaller than 0.01 eV/Å. The convergence criterion of electronic relaxation is 10^{-6} eV for the bulk and pristine surface calculation and 10^{-4} eV for the vacancies calculations. The Gaussian smearing method was used for density of states calculations with a smearing width of 0.02 eV. The k -mesh for the DOS calculation is $7 \times 7 \times 1$.

3. Results and Discussions

Firstly, we calculated the electronic structures of bulk $\text{Co}_3\text{Sn}_2\text{S}_2$. This compound possesses a quasi-two-dimensional structure with the Co_3 -Sn layer sandwiched by Sn and S layers, as shown in Fig. 1a. The lattice parameters calculated with various functionals are summarized and compared with previous works in Supporting Material Table S1. We calculated the band structures and magnetic moments in a primitive cell with different functionals. The magnetic moments calculated with LDA, PBE, meta-GGA, and hybrid functionals applied are summarized in Supporting Material Table S2. The band structures are calculated along high symmetry paths in the first Brillouin zone, as shown in Fig. 1e.

The spin-polarized band structures in a $\text{Co}_3\text{Sn}_2\text{S}_2$ primitive cell with PBE functional is shown in Fig. 1b. The separation of spin-up and spin-down channels indicates a ferromagnetic order and the magnetic moment is $0.35 \mu_B$ on each Co atom, which is consistent with previous experiments^[24]. The valence and conductance bands inverse and form a nodal-ring, which is shown as a pair of crossing points close to the Fermi level in the spin-down channel near the L point. Then the nodal-ring decay into a pair

of Weyl points when spin-orbital coupling (SOC) is considered, as shown in Fig. 1f. A small gap is opened near the L point because the Weyl points are very close to the high symmetry line but not in it. The position of the nodal-ring and Weyl points are highly consistent with previous works [16].

We also calculated the electronic structures of bulk $\text{Co}_3\text{Sn}_2\text{S}_2$ with functionals at higher levels of the Jacob ladder, which most of time generates better electronic structures near the Fermi level. The band structures calculated with the mBJ functional are shown in Fig. 1c and 1g. It is clearly shown that only one crossing point near the U point remains and the other one is missed. For the HSE06 functional, a gap appears near the Fermi level in the spin-polarized band structure, as shown in Fig. 1d, which is different from the experimental observation. Moreover, the HSE06 functional highly overestimate the magnetism of $\text{Co}_3\text{Sn}_2\text{S}_2$. The magnetic moment calculated with HSE06 functional is $0.48 \mu_B$ on each Co atom, which is nearly 50 % larger than the experimental reported value. Considering the fact that $\text{Co}_3\text{Sn}_2\text{S}_2$ possesses a moderate electronic correlation [19], this significant deviation may contribute to the overestimation of the electronic correlation strength by these functionals. Thus, considering the position of Weyl points and the calculated magnetic moments, we found that the semi-empirical PBE functional captures both features among all the functionals, so it is exploited for later investigations.

We then calculated the surface energies of surfaces with different terminations, which determines whether a surface is easy to cleave. The surface energies are calculated using the following formula:

$$\gamma_s = \frac{1}{2A}(E_s^{unrelax} - NE_b) + \frac{1}{A}(E_s^{relax} - E_s^{unrelax})$$

Where A is the surface area, $E_s^{unrelax}$ and E_s^{relax} are the energies of the unrelaxed and relaxed surfaces, respectively. N is the number of atoms in the slab model and E_b is the energy per atom of bulk compounds [48].

The surface energies of S-terminated, Sn-terminated, and Co-terminated surfaces are summarized in Supporting Material Table S3. It is found that Co-terminated surfaces possess the highest surface energy of $0.080 \text{ eV}/\text{\AA}^2$ among three surfaces, which is close to the value of Si(111) surface^[49]. It indicates that Co-terminated surfaces are hard to cleave, which explained the fact that the Co-terminate surface is hard to find experimentally. While for Sn-terminated and S-terminated surfaces, the surface energies are $0.034 \text{ eV}/\text{\AA}^2$ and $0.032 \text{ eV}/\text{\AA}^2$, respectively, which are larger than that of graphite^[50], but are close to that of the $\text{YBa}_2\text{Cu}_3\text{O}_7$ (001) surface^[51]. The surface energies of S-terminated and Sn-terminated surfaces are half the value of Co-terminated surface. The reason is that to form S-terminated and Sn-terminated surfaces, only three Co-Sn bonds need to be broken. While for a Co-terminated surface, besides three Co-Sn bonds, extra three Co-S bonds are also need to be broken. And the Co-S bond is stronger than the Co-Sn bond, which can be estimated by its smaller bond length.

Then we investigate the formation energies of S vacancies that appear in the S-terminated surface. According to the surface energy calculations, S-terminated surfaces are easy to cleave. Indeed, these surfaces are frequently observed in experiments^[15, 17, 39, 52] with randomly distributed S vacancies, including mono-sulfur vacancy (V_S), di-sulfur vacancy (V_{S_2}), and tri-sulfur vacancy (V_{S_3}). The formation energies of different types of S vacancies are summarized in Table 1. The formation energies of different defects were calculated using the following formulas:

$$E_f = E_{\text{defect}} + \sum_i n_i \mu_i - E_{\text{perfect}}$$

where E_{defect} (E_{perfect}) is the total energy of the system with (without) defects. n_i is the number of atoms being removed from the host. And μ_i is the chemical potential of the removed atom. The range of the chemical potentials are in the range of:

$$\frac{1}{2}(E_{\text{Co}_3\text{Sn}_2\text{S}_2} - 2E_{\text{Sn}} - 3E_{\text{Co}}) \leq \mu_S \leq E_S$$

$$\frac{1}{2}(E_{\text{Co}_3\text{Sn}_2\text{S}_2} - 2E_S - 3E_{\text{Co}}) \leq \mu_{\text{Sn}} \leq E_{\text{Sn}}$$

where E_S , E_{Sn} , and E_{Co} are the energy per atom of S, Sn, and Co in pure bulk form.

$E_{\text{Co}_3\text{Sn}_2\text{S}_2}$ is the total energy of the bulk $\text{Co}_3\text{Sn}_2\text{S}_2$ unit cell.

After losing a S atom on a S-terminated surface, three Co atoms underneath the vacancy site are exposed, as shown in Fig. 2a. A kinetic energy cutoff of 270 eV was used for defective surface calculations. The three Co atoms are displaced slightly inward. The distance between the neighboring Co atoms changes from 2.58 Å in a pristine S-terminated surfaces to 2.51 Å after the formation of a V_S . The formation energy of V_S on the S-terminated surface is 2.36 eV at the S-rich limit and 1.14 eV at the S-poor limit, which is smaller than that of V_S in monolayer MoS_2 and WS_2 ,^[53, 54] leading to a larger chance to form V_S on S-terminated surfaces.

The electronic structures of V_S were calculated, which is shown in Fig. 2b. Two bands appear inside the gap near Fermi level at the spin-down channel, which are degenerate at the Γ point and almost degenerate with only 1~2 meV energy difference at M and K points. The localized density of states (LDOS) at the vacancy site, which is shown in Fig. 2c, clearly shows a peak at the spin-down channel with the energy of 0.05 eV above the Fermi level. These results indicate that V_S on the S-terminated surface induces a magnetic localized bound state inside the gap of the spin-down channel near the Fermi level.

The interactions of V_S were then investigated. The formation energies of a di-sulfur-vacancy (V_{S2}) and a tri-sulfur-vacancy (V_{S3}) in different configurations are shown in Table 1. It is found that the formation energies of V_{S2} and V_{S3} are almost twice and three times that of V_S , respectively, suggesting that the interactions between S vacancies are not strong. This small energy difference among V_S , V_{S2} , and V_{S3} may explain the random distribution of sulfur vacancies in STM images of the S-terminated surface^[15, 20].

Though the interaction between neighboring S vacancies do not significantly lower the formation energy, it strongly affects the localized bound states inside the energy gap. The atomic structure of V_{S2} is shown in Fig. 2d. The electronic structures of the

S-terminated surface with di-vacancies are shown in Fig. 2e and 2f. The band structure and the LDOS indicate that two defect states appear inside the gap near the Fermi level. Each defect state contains two almost degenerate bands. The energies of these two localized bond states are 0.04 eV and 0.08 eV higher than the gap edge, pointed out by the red and green arrow in Fig. 2f. Interestingly, the localized bond state of V_S is 0.06 eV higher than the gap edge, in the middle of the two localized bond states of V_{S_2} . So these two defect states in V_{S_2} are more likely to be the consequence of the orbital hybridizations of the defect state of V_S .

The spatial distributions of the two localized states induced by the sulfur vacancies are plotted in Fig. 2g and 2h. As shown in Fig. 2g, there is a significant electron accumulation between the two sulfur vacancy sites, indicating that the defect state sitting at 0.04 eV above the gap edge (red arrow in Fig. 2f) presents a bonding orbital feature. While, as shown in Fig. 2f, the charge distribution of the defect state sitting at 0.08 eV above the gap edge (green arrow in Fig. 2f) reflects an anti-bonding orbital feature. Thus, we conclude that when two V_S in V_{S_2} interact with each other, the localized bond states hybridize and form a bonding state as well as an anti-bonding state. It should be mentioned that, because the isolated defect level is unoccupied, although the energy is lowered by the hybridization, the bounding state is still above the Fermi level.

Then we considered three sulfur vacancies cases. The three sulfur vacancies are built in two ways, triangular shape and linear shape. The triangle V_{S_3} contains three S vacancies combined in an equilateral triangle, as shown in Fig. 3a. The band structure of triangle V_{S_3} , as shown in Fig. 3b, also shows two group defect states inside the gap near the Fermi level. Different from the feature in V_{S_2} case, the defect state near the band edge shows a significant broadened bandwidth. The LDOS project on the vacancy site, which is shown in Fig. 3c, shows two peaks at the energy of 0.04 and 0.13 eV above the Fermi level, respectively. Obviously, the peak marked by the red arrow is much broader.

The line V_{S3} contains three S vacancies in a row, as shown in Fig. 3d. The band structure of line V_{S3} (Fig. 3e) shows that the defect states are further broadened and split. The LDOS projected on the vacancy site is shown in Fig. 3f. Besides the two peaks with the energy of 0.05 and 0.14 eV above the Fermi level (red and green arrow in Fig. 3f), there is a small bump in between, representing the splitting of the defect states. The electronic structure of line V_{S3} is more complicated than that of triangle V_{S3} and that may account for the lower symmetric configuration of line V_{S3} . It is also noting that the energy differences between the two peaks in LDOS of the triangle and line V_{S3} are both 0.09 eV, larger than that in the V_{S2} case (0.04 eV). The increasing energy splitting of the bonding states and the anti-bonding states indicates that the interaction between the V_S in V_{S3} is larger than that of V_{S2} .

The charge density distributions of the defect states in V_{S3} were then calculated. The charge density distribution of the lower defect states (marked by the red arrows in Figs. 3c and 3f) shows a bonding orbital feature (Supporting Material Figs. S1a and S1c). The higher energy defect states (marked by the green arrows in Figs. 3c and 3f) shows an anti-bonding orbital feature (Supporting Material Figs. S1b and S1d). Thus, we conclude that the orbital hybridization and the formation of the bonding/anti-bonding states are universal features when sulfur vacancies are closed to each other.

We then considered the single Sn vacancy on a Sn-terminated surface. The atomic structure is shown in Fig. 4a. The formation energy is 0.41 eV at the Sn-rich limit and -0.81 eV at the Sn-poor limit. The band structure of a Sn-terminated surface with a Sn vacancy is shown in Fig. 4b. From the band structure calculations, it is found that the Sn-terminated surface with a V_{Sn} is a semimetal with a 0.4 eV bandgap in the spin-down channel. It is also found that there is no the defect state in the gap of the spin-down channel. By checking the LDOS plot projected on the vacancy site (as shown in Fig. 4c), we found that a peak at the energy of -0.35 eV, indicating that the

defect level is merged with the valence band of the surface.

The charge density distributions decomposed to different energies were analyzed to identify the defect states. As shown in Fig. 4d, the spatial distribution of the peak at -0.35 eV (marked by the blue arrow in Fig. 4c) reveals a three-fold feature around the Sn vacancy. This indicates that the defect states induced by a single Sn vacancy are also localized bond states. The side view of the spatial charge density distribution around the peak of the defect states, which is shown in Fig. 4e, indicates that the charge distributes on the top two layers. The spin-polarized projected density of states (PDOS) on surface atoms, as shown in Fig. 4f, also shows a peak with the energy of -0.35 eV, corresponding to the energy of the defect states. So, the localized bound states induced by the Sn vacancy is merged with the trivial valence band.

4. Conclusion and perspectives

We calculated band structures and magnetic moments of bulk $\text{Co}_3\text{Sn}_2\text{S}_2$ with functionals at different levels. It is found that GGA functional in the PBE form reproduces the positions of Weyl points observed in previous experiments. We then investigate the influence of vacancies on the electronic structure of S-terminated and Sn-terminated surfaces. For S-terminated surfaces, a localized bond state induced by V_S was found inside the gap. When V_S combined and interacted with each other, the localized bond states hybridize and generate bonding states as well as anti-bonding states. For Sn-terminated, localized states are merged inside the valence band, thus not observed near the Fermi level.

References

1. Liu D F, Liang A J, Liu E K, Xu Q N, Li Y W, Chen C, Pei D, Shi W J, Mo S K, Dudin P, Kim T, Cacho C, Li G, Sun Y, Yang L X, Liu Z K, Parkin S S P, Felser C and Chen Y L 2019 *Science* **365** 1282
2. Liu C, Shen J L, Gao J C, Yi C J, Liu D, Xie T, Yang L, Danilkin S, Deng G C, Wang W H, Li S L, Shi Y G, Weng H M, Liu E K and Luo H Q 2021 *Sci. China-Phys. Mech. Astron.* **64** 217062
3. Shvetsov O O, Esin V D, Barash Y S, Timonina A V, Kolesnikov N N and Deviatov E V 2020 *Phys. Rev. B* **101** 035304
4. Howard S, Jiao L, Wang Z Y, Vir P, Shekhar C, Felser C, Hughes T and Madhavan V 2019 arXiv:1910.11205
5. Fujiwara K, Ikeda J, Shiogai J, Seki T, Takanashi K and Tsukazaki A 2019 *Jpn. J. Appl. Phys.* **58** 050912
6. Shi Q, Zhang X, Yang E, Yan J, Yu X Y, Sun C, Li S and Chen Z W 2018 *Results*

Phys. **11** 1004

7. Mangelis P, Vaqueiro P, Jumas J-C, da Silva I, Smith R I and Powell A V 2017 *J. Solid State Chem.* **251** 204
8. Lv B Q, Xu N, Weng H M, Ma J Z, Richard P, Huang X C, Zhao L X, Chen G F, Matt C E, Bisti F, Strocov V N, Mesot J, Fang Z, Dai X, Qian T, Shi M and Ding H 2015 *Nat. Phys.* **11** 724
9. Xu S Y, Belopolski I, Alidoust N, et al. 2015 *Science* **349** 613
10. Weng H M, Fang C, Fang Z, Bernevig B A and Dai X 2015 *Phys. Rev. X* **5** 011029
11. Vaqueiro P and Sobany G G 2009 *Solid State Sci.* **11** 513
12. Kassem M A, Tabata Y, Waki T and Nakamura H 2017 *Phys. Rev. B* **96** 014429
13. Yan W N, Zhang X, Shi Q, Yu X Y, Zhang Z Q, Wang Q, Li S and Lei H C 2018 *Solid State Commun.* **281** 57
14. Sugawara A, Akashi T, Kassem M, Tabata Y, Waki T and Nakamura H 2019 *Phys. Rev. Mater.* **3** 104421
15. Morali N, Batabyal R, Nag P K, Liu E K, Xu Q N, Sun Y, Yan B H, Felser C, Avraham N and Beidenkopf H 2019 *Science* **365** 1286
16. Xu Q N, Liu E K, Shi W J, Muechler L, Gayles J, Felser C and Sun Y 2018 *Phys. Rev. B* **97** 235416
17. Jiao L, Xu Q N, Cheon Y, Sun Y, Felser C, Liu E K and Wirth S 2019 *Phys. Rev. B* **99** 245158
18. Li G W, Xu Q N, Shi W J, Fu C G, Jiao L, Kamminga M E, Yu M Q, Tüysüz H, Kumar N, Süß V, Saha R, Srivastava A K, Wirth S, Auffermann G, Gooth J, Parkin S, Sun Y, Liu E K and Felser C 2019 *Sci. Adv.* **5** eaaw9867
19. Yang R, Zhang T, Zhou L Q, Dai Y M, Liao Z Y, Weng H M and Qiu X G 2020 *Phys. Rev. Lett.* **124** 077403
20. Liu E K, Sun Y, Kumar N, et al. 2018 *Nat. Phys.* **14** 1125
21. Wang Q, Xu Y F, Lou R, Liu Z H, Li M, Huang Y B, Shen D W, Weng H M, Wang S C and Lei H C 2018 *Nat. Commun.* **9** 3681
22. Chen X L, Wang M Y, Gu C C, Wang S Y, Zhou Y H, An C, Zhou Y, Zhang B W, Chen C H, Yuan Y F, Qi M Y, Zhang L L, Zhou H D, Zhou J H, Yao Y G and Yang Z R 2019 *Phys. Rev. B* **100** 165145
23. Geishendorf K, Schlitz R, Vir P, Shekhar C, Felser C, Nielsch K, Goennenwein S T B and Thomas A 2019 *Appl. Phys. Lett.* **114** 092403
24. Guguchia Z, Verezhak J A T, Gawryluk D J, et al. 2020 *Nat. Commun.* **11** 559
25. Yang S-Y, Noky J, Gayles J, Dejene F K, Sun Y, Dörr M, Skourski Y, Felser C, Ali M N, Liu E K and Parkin S S P 2020 *Nano Lett.* **20** 7860
26. Ding L C, Koo J, Xu L C, Li X K, Lu X F, Zhao L X, Wang Q, Yin Q W, Lei H C, Yan B H, Zhu Z W and Behnia K 2019 *Phys. Rev. X* **9** 041061
27. Geishendorf K, Vir P, Shekhar C, Felser C, Facio J I, van den Brink J, Nielsch K, Thomas A and Goennenwein S T B 2020 *Nano Lett.* **20** 300
28. Guin S N, Vir P, Zhang Y, Kumar N, Watzman S J, Fu C G, Liu E K, Manna K, Schnelle W, Gooth J, Shekhar C, Sun Y and Felser C 2019 *Adv. Mater.* **31** 1806622
29. Qiao Q, Zhang Y-Y, Contreras-Guerrero R, Droopad R, Pantelides S T,

- Pennycook S J, Ogut S and Klie R F 2015 *Appl. Phys. Lett.* **107** 201604
30. Zhou W, Zhang Y-Y, Chen J Y, Li D D, Zhou J D, Liu Z, Chisholm M F, Pantelides S T and Loh K P 2018 *Sci. Adv.* **4** eaap9096
31. Xu H K and Ouyang G 2020 *Chin. Phys. B* **29** 37302
32. Reshchikov M A and Morkoc H 2005 *J. Appl. Phys.* **97** 95
33. Li L, Yang L-A, Zhou X-W, Zhang J-C and Hao Y 2013 *Chin. Phys. B* **22** 87104
34. Zhao X X, Fu D Y, Ding Z J, Zhang Y-Y, Wan D Y, Tan S J R, Chen Z X, Leng K, Dan J D, Fu W, Geng D C, Song P, Du Y H, Venkatesan T, Pantelides S T, Pennycook S J, Zhou W and Loh K P 2018 *Nano Lett.* **18** 482
35. Yang S Z, Gong Y J, Manchanda P, Zhang Y Y, Ye G L, Chen S M, Song L, Pantelides S T, Ajayan P M, Chisholm M F and Zhou W 2018 *Adv. Mater.* **30** 7
36. Gao T, Kumar A, Shang Z, Duan X, Wang H, Wang S, Ji S, Yan D, Luo L, Liu W and Sun X 2019 *Chin. Chem. Lett.* **30** 2274
37. Hu K, Ming C, Liu Y, Zheng C, Zhang S, Wang D, Zhao W and Huang F 2020 *Chin. Chem. Lett.* **31** 2809
38. Yin J X, Shumiya N, Jiang Y X, et al. 2020 *Nat. Commun.* **11** 4415
39. Xing Y Q, Shen J L, Chen H, et al. 2020 *Nat. Commun.* **11** 5613
40. Kresse G and Furthmüller J 1996 *Comput. Mater. Sci.* **6** 15
41. Kresse G and Furthmüller J 1996 *Phys. Rev. B* **54** 11169
42. Blöchl P E 1994 *Phys. Rev. B* **50** 17953
43. Perdew J P, Burke K and Ernzerhof M 1996 *Phys. Rev. Lett.* **77** 3865
44. Becke A D and Johnson E R 2006 *J. Chem. Phys.* **124** 221101
45. Tran F and Blaha P 2009 *Phys. Rev. Lett.* **102** 226401
46. Krukau A V, Vydrov O A, Izmaylov A F and Scuseria G E 2006 *J. Chem. Phys.* **125** 224106
47. Monkhorst H J and Pack J D 1976 *Phys. Rev. B* **13** 5188
48. Li Q, Rellán-Piñeiro M, Almora-Barrios N, Garcia-Ratés M, Remediakis I N and López N 2017 *Nanoscale* **9** 13089
49. Stekolnikov A A, Furthmüller J and Bechstedt F 2002 *Phys. Rev. B* **65** 115318
50. Wang W, Dai S Y, Li X D, Yang J R, Srolovitz D J and Zheng Q S 2015 *Nat. Commun.* **6** 7853
51. Miletto, Granozio F and di Uccio U S 1997 *J. Cryst. Growth* **174** 409
52. Yin J X, Zhang S S, Chang G Q, et al. 2019 *Nat. Phys.* **15** 443
53. Hong J H, Hu Z X, Probert M, Li K, Lv D H, Yang X N, Gu L, Mao N N, Feng Q L, Xie L M, Zhang J, Wu D Z, Zhang Z Y, Jin C H, Ji W, Zhang X X, Yuan J and Zhang Z 2015 *Nat. Commun.* **6** 8
54. Li W F, Fang C M and van Huis M A 2016 *Phys. Rev. B* **94** 8

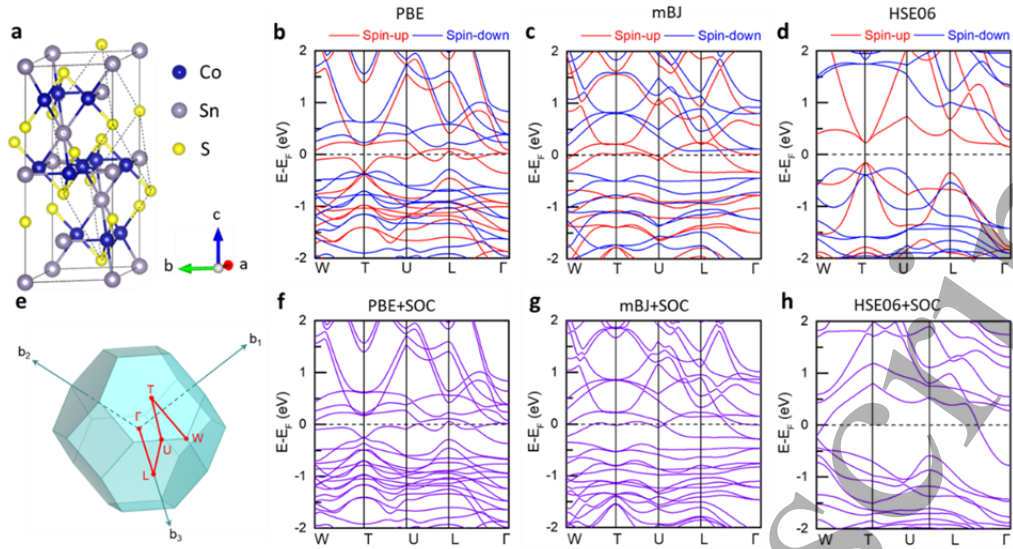


Fig. 1. The atomic structure and electronic structures of bulk $\text{Co}_3\text{Sn}_2\text{S}_2$. (a) The atomic structure of $\text{Co}_3\text{Sn}_2\text{S}_2$ in a conventional cell containing three formulas. The dashed line indicates primitive cell of $\text{Co}_3\text{Sn}_2\text{S}_2$. The blue, grey and yellow balls represent Co, Sn, and S atoms, respectively. (b)-(d) Spin-polarized band structures of $\text{Co}_3\text{Sn}_2\text{S}_2$ in primitive cell with PBE, mBJ, and HSE06 functionals, respectively. (e) The first Brillouin zone showing high symmetry paths. (f)-(h) Band structures of $\text{Co}_3\text{Sn}_2\text{S}_2$ considering spin-orbital coupling with PBE, mBJ, and HSE06 functionals, respectively.

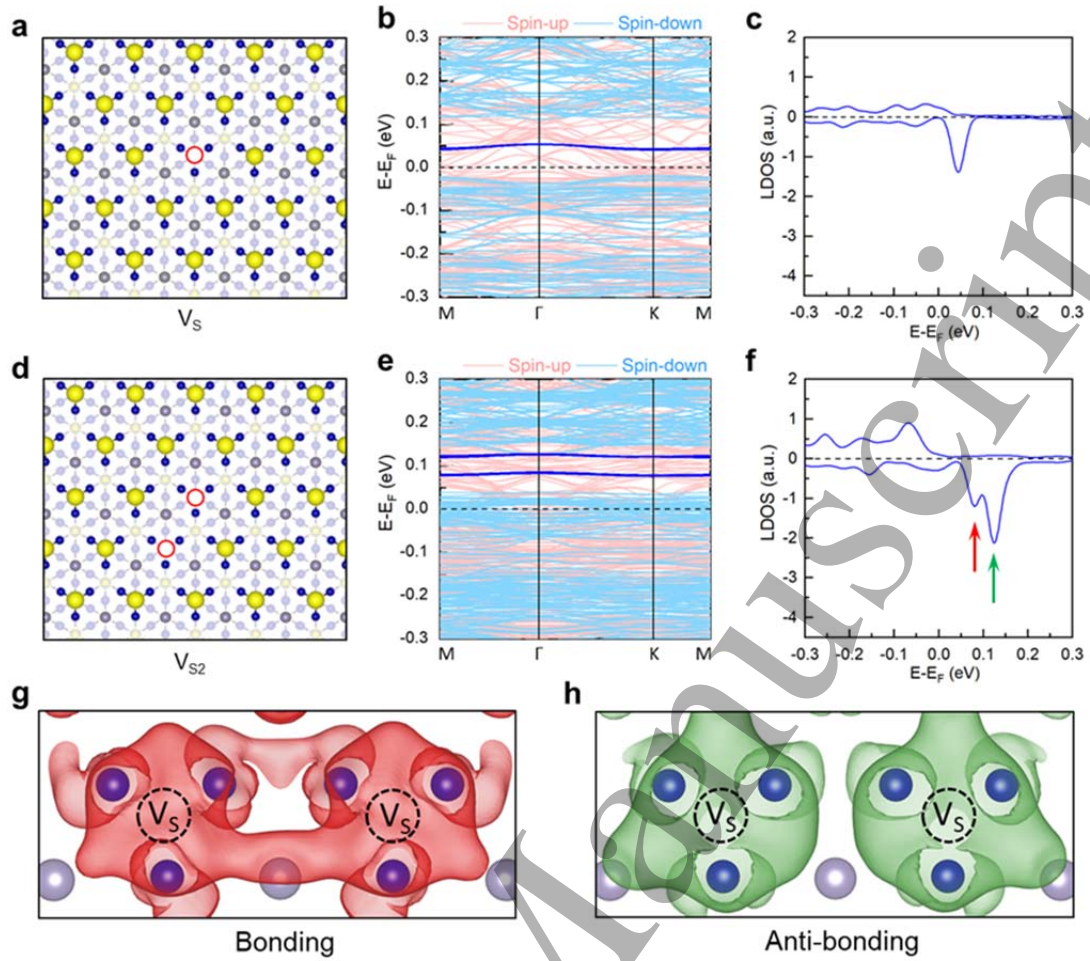


Fig. 2. Localized bond states induced by V_S and V_{S2} at a S-terminated surface of $\text{Co}_3\text{Sn}_2\text{S}_2$. (a) The atomic configuration of a S-terminated surface containing a V_S . The red hollow circle represents the S vacancy. (b) The band structure of the S-terminated surface with a V_S . The dark blue lines are the localized bound states. (c) Spin-polarized localized density of states (LDOS) projected on V_S . (d) The atomic structure of a S-terminated surface with V_{S2} . (e) The band structure of the S-terminated surface with V_{S2} . (f) Spin-polarized LDOS projected on V_{S2} . The two defect states are labeled by red and green arrows. (g) and (h) The charge distribution of the two defect states marked by the red and green arrow in (f), respectively. An isosurface of $8.0 \times 10^{-5} e/\text{Bohr}^3$ is used.

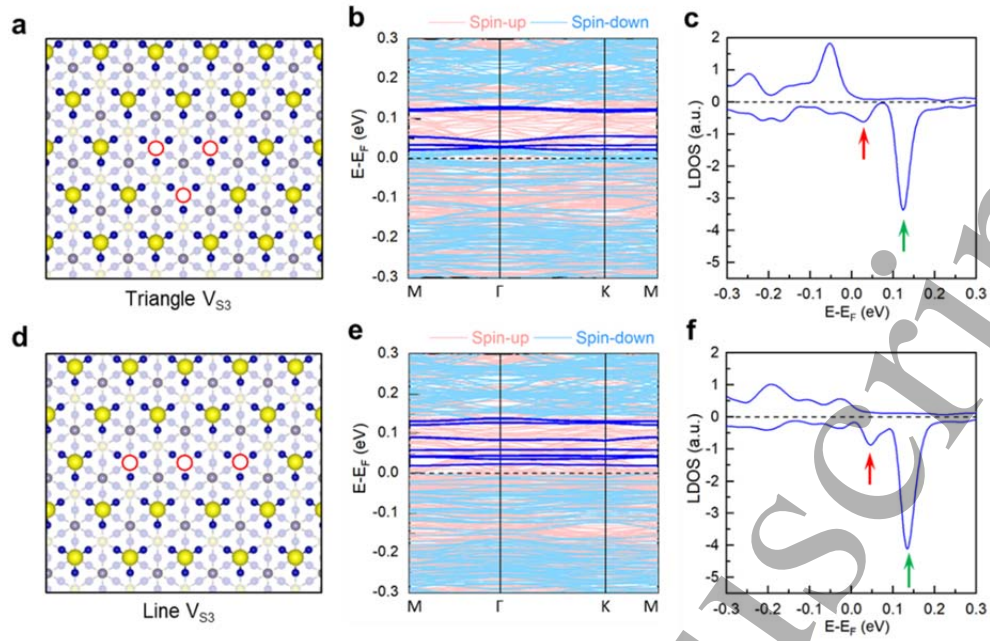


Fig. 3. Localized defect states induced by three sulfur vacancies at the S-terminated surface of $\text{Co}_3\text{Sn}_2\text{S}_2$. (a)-(c) The atomic configuration, band structure, and LDOS of a S-terminated surface with three sulfur vacancies in a triangular shape. (d)-(f) The atomic configuration, band structure, and LDOS of a S-terminated surface with three sulfur vacancies in a linear shape. The two groups of defect states are labeled by red and green arrows in (c) and (f).

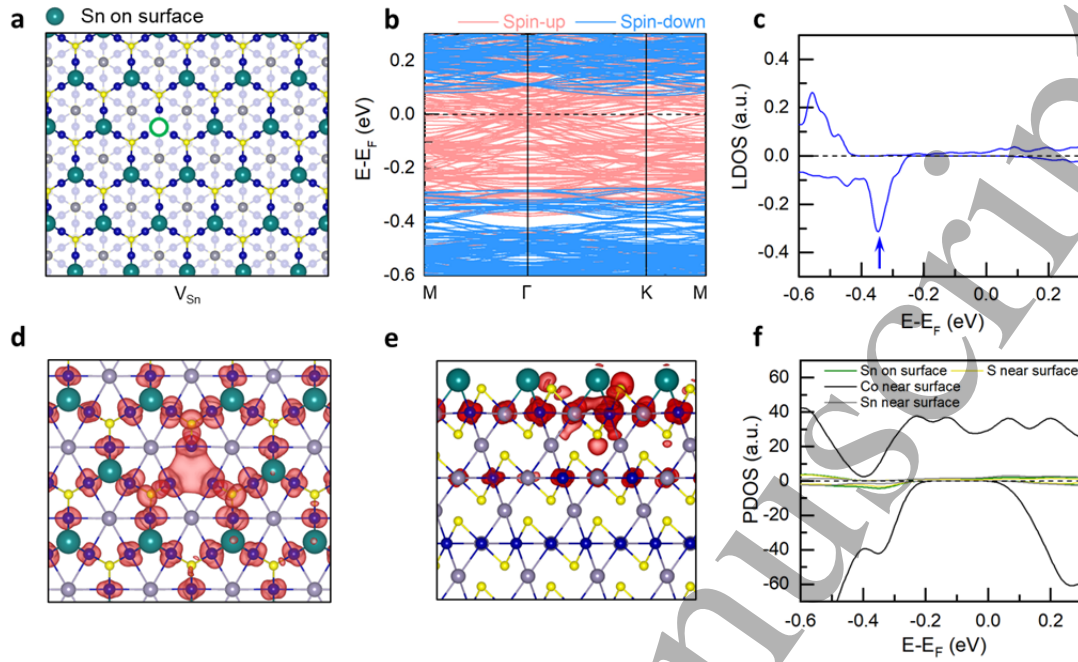


Fig. 4. Electronic structure of the Sn-terminated surface with a single Sn vacancy. (a) The atomic structure of a Sn-terminated surface with a V_{Sn} . Big green balls represent the top-layer Sn atoms and the green hollow circle represents the single Sn vacancy. (b) The band structure of the Sn-terminated surface with V_{Sn} . (c) Spin-polarized LDOS projected on the Sn vacancy site. (d) and (e) Top and side views of the charge distribution of the defect state marked by the blue arrow in (c), respectively. An isosurface of $8.0 \times 10^{-5} e/\text{Bohr}^3$ is used. (f) Spin-polarized projected density of states (PDOS) of Sn atoms on the surface as well as Co, Sn, and S atoms near surface.

Table 1. Formation energies of vacancies on $\text{Co}_3\text{Sn}_2\text{S}_2$ surfaces with different terminations.

| Defect types | Formation energy (eV) | | |
|---------------|-----------------------|------------|-------|
| | Rich-limit | Poor-limit | |
| S-terminated | V_S | 2.36 | 1.14 |
| | V_{S2} | 4.84 | 2.39 |
| | Triangle V_{S3} | 7.20 | 3.53 |
| | Line V_{S3} | 7.18 | 3.51 |
| Sn-terminated | Single V_{Sn} | 0.41 | -0.81 |